Spring 2010

Graded-index fiber collimator enhanced extrinsic Fabry-Perot interferometer

Yinan Zhang

Department:

GRADED-INDEX FIBER COLLIMATOR ENHANCED EXTRINSIC FABRY-PEROT INTERFEROMETER

by

YINAN ZHANG

A THESIS

Presented to the Faculty of the Graduate School of the

MISSOURI UNIVERSITY OF SCIENCE AND TECHNOLOGY

In Partial Fulfillment of the Requirements for the Degree

MASTER OF SCIENCE IN ELECTRICAL ENGINEERING

2010

Approved by

Dr. Hai Xiao, Advisor
Dr. Steve E. Watkins
Dr. Hai-Lung Tsai

ABSTRACT

In this thesis, we studied a fringe visibility enhanced extrinsic Fabry-Perot interferometer (EFPI) by fusion splicing a quarter-pitch graded-index fiber (GIF) fiber to the lead-in single-mode fiber (SMF). The performance of the GIF collimator is theoretically analyzed using a ray matrix model and experimentally verified through beam divergence angle measurements. The fringe visibility of the GIF-collimated EFPI is measured as a function of the cavity length and compared with that of a regular SMF-EFPI. At the cavity length of 500 μm, the fringe visibility of the GIF-EFPI is 0.8 while that of the SMF-EFPI is only 0.2. The visibility enhanced GIF-EFPI provides better a signal-to-noise (SNR) for applications where a large dynamic range is desired.

ACKNOWLEDGMENTS

I would like to take this opportunity to thank all those people who helped me with the successful completion of my research. First, I would like to express my gratitude to my advisor Dr. Hai Xiao, without who this research could be considered incomplete. I thank him for giving me a chance to work with him and for his continued support with valuable advice and encouragement. His subtle guidance with unbelievable patience has made a great impact on this research and me.

I am grateful to Dr. Steve E. Watkins, Department of Electrical and Computer Engineering and Dr. Hai-Lung Tsai, Department of Mechanical and Aerospace Engineering for being my committee members. And I would like to thank Dr. Genda Chen, Department of Civil Engineering, for support and guidance of this project.

I own a great deal of gratitude to Ying Huang, Tao Wei, Xinwei Lan, Yanjun Li, Sudha Sneha Devarakonda and Hongbiao Duan, who worked with me on this research project and gave me a lot of help and advice.

I would also like to thank my parents for everything they have done for me. Finally, I would like to thank the sponsors for this project. They are the U.S. National Science Foundation, the Mid-America Transportation Center and the U.S. Department of Energy – National Energy Technology Laboratory.

TABLE OF CONTENTS

Page

LIST OF ILLUSTRATIONS

LIST OF ABBRIVIATIONS

Abbreviation	Full name
ASE	Amplified-spontaneous-emission
EFPI	Extrinsic Fabry-Perot Interferometer
EMI	Electromagnetic interference
FDTD	Finite-difference time-domain
GIF	Graded-index fiber
GRIN	Gradient-index
IFPI	Intrinsic Fabry-Perot Interferometer
ID	Inner diameter
MEMS	Micro-Electro-Mechanical Systems
MFD	Mode field diameter
NA	Numerical aperture
OCT	Optical coherence tomography
SMF	Single-mode fiber
SHM	Structural health monitoring
SNR	Signal-to-noise ratio

1. INTRODUCTION

1.1. BACKGROUND

Under extreme loads such as earthquakes and landslides, civil structures often experience excessive deformations or strains in the order of 10,000με to 100,000με. To address the recent needs for the progressive collapse study of structural systems under extreme loads, large strain measurements are of paramount importance. Implementation of successful SHM requires selection of sensors that are capable to work in harsh environment and compatible with the materials and scope of measurements.

Development of large strain sensors has recently attracted worldwide attention. To this endeavor, the main challenge remains in achieving both a large dynamic range and a high resolution of strain measurement. Conventional strain sensors represented by electro-resistive strain gauges have a satisfactory resolution of 4~10 με but a limited dynamic range of less than 15,000 με or 1.5%. For strains higher than 2%, extensometers, linear variable differential transformers [1] , and grating based mark tracking technique [2] are commonly used. They can typically measure a strain of up to 5% with a low resolution of larger than 4,500με or 0.45%.

1.2. EFPI SENSORS FOR STRAIN SENSING

Optical fiber-inline EFPI have found many sensing applications in recent years [3]. An EFPI device can be easily made by packaging two cleaved optical fibers into a capillary tube, leaving an air gap between the two fiber endfaces. Reflections of light from the two cleaved fiber surfaces form an interference signal that can be recorded and processed to find the cavity length. When used as a sensor, the optical path length (i.e., the product of the cavity length and the refractive index of the medium filling the cavity) changes as a function of the parameters to be measured. With proven advantages such as immunity to EMI, high resolution, multiplexing capability, small size, and structural ruggedness, EFPI sensors have been demonstrated for measurement of a wide variety of parameters including temperature [4], strain [5], pressure [6], displacement [7], ultrasound [8], magnetic field [9], and refractive index [10].

Based on the structure of Fabry-Perot cavity, people divide Fabry-Perot interferometers to two categories: IFPI and EFPI. In an IFPI sensor, a cavity is formed between two partial mirrors placed inside the fiber [11]. While in an EFPI sensor, the Fabry-Perot cavity is outside of the fiber. The EFPIs are used more than the IFPIs because of their flexibility of fabrication and application [12].

Fig. 1.1 (a) shows the schematic structure of an EFPI sensor head. The sensor head consists of two optical fibers encapsulated in a silica tube. The fiber and the silica tube are bonded together by CO_2 laser irradiation, as shown in Fig. 1.1 (b). The cleaved endfaces of the two fibers compose a low finesse EFPI. The silica tube serves two important functions. First, it provides a robust package to physically and optically protect the encapsulated fibers. Second, by varying the inner and outer diameter as well as the length of the tube, the sensitivity and dynamic range of the sensor can be tuned to its optimal values.

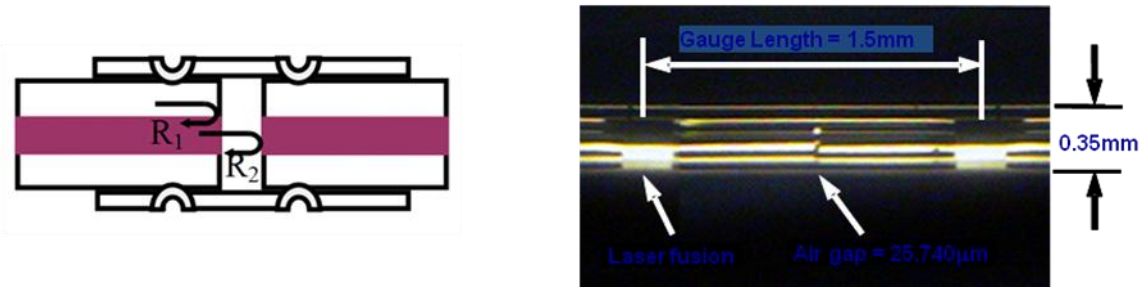

Figure 1.1. The structure of EFPI sensor head. (a) Schematic drawing of EFPI, (b) Microscopic image of EFPI.

EFPI has been employed for strain sensing in recent decades. Claus *et al*. reported an EFPI sensor for strain and crack opening displacement measurement from -200 to 900 ℃ [13]. This particular sensor works properly within a dynamic range of 1% and has a resolution of as high as 1με. Seat *et al*. used a dual-cavity EFPI sensor to determine dynamic displacement with a measurement range up to 139 μm [14].

A photograph of tension test using EFPI sensor is shown in Fig. 1.2 and Fig. 1.3. The EFPI was encapsulated in a glass tube and attached to a steel specimen, along with a conventional strain gauge.

Figure 1.2. Strain measurement using EFPI sensor

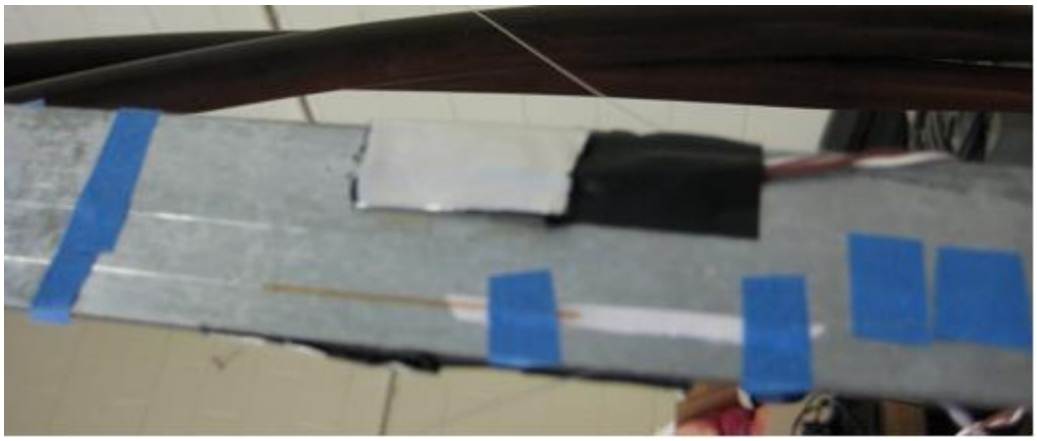

Figure 1.3. EFPI and strain gauge attached to steel structure

1.3. GIF EFPI SENSORS FOR LARGE STRAIN MEASUREMENT.

SMF EFPI sensor has a fringe visibility decreasing rapidly as its cavity length increases due to the divergence (typically about 8 °) of the exit beam from the optical fiber. The decreasing fringe visibility could result in a limited maximum initial cavity length, small dynamic range, and reduced SNR for certain applications where a long initial cavity length or large dynamic range is required, for example, crack and fracture monitoring in SHM. In general, the fringe visibility of EFPI is determined by fiber core size, NA, modal power distribution in the lead-in fiber, and cavity length. One way of improving fringe visibility is to minimize the NA of the lead-in fiber so that the divergence angle of the exit beam becomes small. Han *et al*. theoretically proved that the fringe visibility of an EFPI with a smaller NA is less sensitive to the gap length of the EFPI sensor.

Gangopadhyay *et al*. reported an EFPI vibration sensor making use of a coated GRIN lens pigtailed to the optical fiber [15]. The use of a GRIN lens not only reduced the divergence angle of the exit beam from an optical fiber but also increased the area of reception for the light reflected from the second endface. As a result, the initial cavity length was large and the dynamic range of the vibration sensor was extended to 65μm. However, pigtailing a GRIN lens to an optical fiber requires additional assembly. The use of a GRIN lens also increases the size of the EFPI sensor and decreases the robustness of the device.

A multimode GIF guides light in a similar way as a GRIN lens does [16]. Alternatively, a small section of GIF can also function as a collimator if the length of the GIF is a quarter of the period (i.e., a quarter-pitch). In fiber optics, a graded-index fiber is an optical fiber whose core has a refractive index that decreases with increasing radial distance from the fiber axis. The most common refractive index profile for a graded-index fiber is very nearly parabolic. The parabolic profile results in continual refocusing of the rays in the core, and minimizes modal dispersion.

Fig. 1.4 displays the refractive index profile of Corning Infinicor 600 GIF. From Fig. 1.4, the maximum refractive index occurs at the center of fiber core, and gradually reduces along the radial axis. In most applications, GIF offers the following properties: relatively high source-to-fiber coupling efficiency, low loss, low sensitivity to micro-

bending and macro-bending, high bandwidth, expansion capability, etc. The GIF based collimators have been demonstrated useful in various applications such as coupling light between an optical fiber and a MEMS device [17], transmitting and collecting light in biomedical imaging [18], and expanding the exit beam from a SMF to excite the cladding modes [19]. Because most of GIFs have the same diameter as that of the SMF (~125μm), they can be easily fusion spliced to a SMF with negligible loss. As such, using a quarter-pitch GIF as the collimator could potentially extend the dynamic range of an EFPI without sacrificing the robustness and increasing the size of the device.

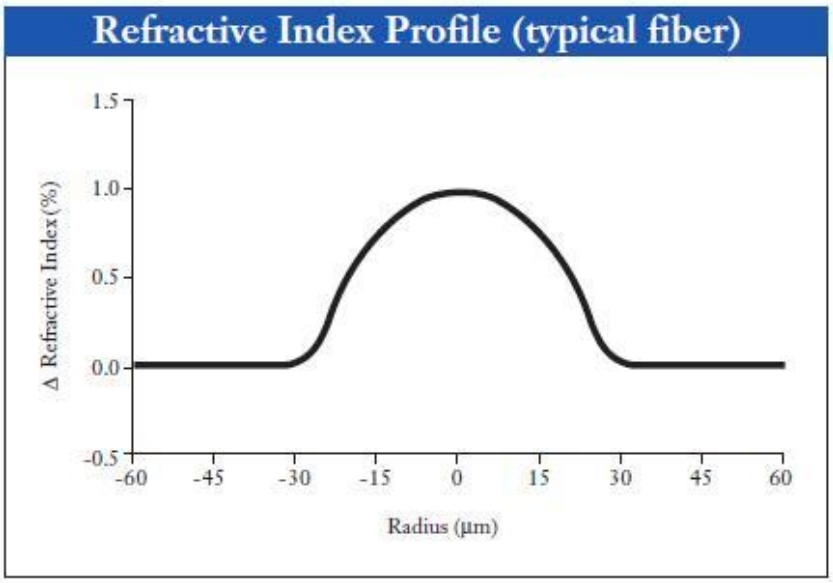

Figure 1.4. Refractive index profile of graded-index fiber

1.4. RESEARCH OBJECTIVE

From the discussion above, the dynamic range of current SMF EFPI sensors are limited for the large strain measurement needed for SHM. Therefore, the main objective of this thesis is to optimize the EFPI sensor design for extended dynamic range.

To be detailed, the specific objectives are:

1. Optimal design of GIF EFPI sensor with extended dynamic range through theoretical analysis and simulation of the fringe visibility,
2. Fabrication and characterization of GIF collimators for smallest divergence angle and implementation of the optimally designed GIF EFPI sensor, and
3. Performance characterization of the newly developed GIF EFPI sensor in comparison with the SMF EFPI sensor.

1.5. THESIS OVERVIEW

This thesis focuses on fringe visibility and dynamic range enhanced GIF EFPI sensor in the application of structural health monitoring. The contents of the thesis are arranged as follows:

Chapter 2 focuses on the principle of low finesse SMF EFPI sensors. Plane wave model is used to describe output light from SMF. Based on the plane wave model, the fringe visibility of a conventional SMF EFPI sensor is derived.

Chapter 3 focuses on the principle and modeling of the proposed low finesse GIF EFPI sensors. The ABCD matrix algorithm [20] is employed to calculate the pitch length of the GIF. The divergence angle of the exit beam of the GIF-pigtailed SMF is experimentally measured and compared with the calculation results.

Chapter 4 describes the construction of the GIF EFPI sensor using a quarter-pitch GIF as a collimator. The fringe visibility enhancement of the GIF EFPI over the SMF EFPI is characterized experimentally.

The conclusions and future work are summarized in Chapter 5.

2. SMF EFPI SENSORS

2.1. PRINCIPLES AND CONFIGURATIONS

The schematic configuration of EFPI sensor is shown in Fig. 2.1. The low-finesse EFPI can be modeled using the following two-beam interference equation [21],

$$P = P_1 + P_2 + 2\sqrt{P_1 P_2}\cos(\frac{4\pi n_0 L}{\lambda} + \varphi_0) \quad (1)$$

where P is the intensity of the interference signal; P_1 and P_2 are the intensities of the reflected light at the two endfaces, respectively; φ_0 is the initial phase of the interference; L is the cavity length; n_0 is the refractive index of the medium filling the cavity (in most cases the medium is air); and λ is the optical wavelength in vacuum.

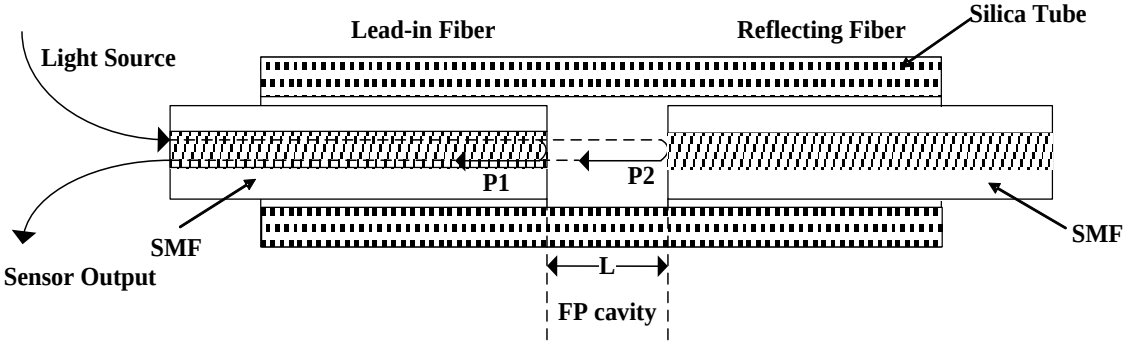

Figure 2.1. Schematic diagram of an EFPI sensor

The intensity of the interference signal reaches its minimum (P_{min}) when the phase of the cosine term in equation 1 becomes an odd number of π. That is,

$$\frac{4\pi L}{\lambda} = (2m+1)\pi \quad (2)$$

where m is an integer.

Since the two adjacent interference minimums have a phase difference of 2π. Therefore the optical length of the cavity L can be calculated by:

$$L = \frac{m\lambda_1\lambda_2}{2(\lambda_2 - \lambda_1)} \tag{3}$$

where λ_1 and λ_2 are the center wavelength of specific interference valleys or peaks.

When an EFPI sensor is subject to external stress, the change of cavity length ΔL as a function of strain can be expressed as [21]

$$\Delta L = \varepsilon L_{gauge} \tag{4}$$

Where ε is the strain applied on the sensor, L_{gauge} is the gauge length of the sensor, which is usually the distance between the two points bonded to the specimen.

2.2. FRINGE VISIBILITY OF SMF EFPI

The quality of the interference signal is commonly quantified by the fringe visibility (or interference contrast), which by definition is given by [22],

$$V = \frac{P_{max} - P_{min}}{P_{max} + P_{min}} \tag{5}$$

where P_{max} and P_{min} are the maximum and minimum intensities of the interference signal, respectively. Derived from Eq. (1) and Eq. (5), the fringe visibility can be expressed as,

$$V = \frac{2\sqrt{P_1 P_2}}{P_1 + P_2} \tag{6}$$

Given the ratio

$$k = \frac{P_2}{P_1} \tag{7}$$

The fringe visibility also writes as,

$$V = \frac{2\sqrt{k}}{1+k} \tag{8}$$

From Equation (1) and (5), the interferometer has a maximum fringe visibility of 1 (or 100%) when the two reflections have an equal intensity ($P_1 = P_2$ or k = 1). However, in most cases, P_2 is smaller than P_1 due to the optical loss of the FP cavity. The difference increases as a function of the cavity length a result of beam divergence. As such, the fringe visibility decreases as the cavity length increases.

2.3. PLANE WAVE MODEL

In theory, the simple structure of EFPI sensor illustrated in Fig. 2.1 will not reach 100 percent. In a typical setup, the reflection from the first fiber-air interface (P_1) is larger than that form the second fiber-air interface (P_2) due to various optical losses inherent to the FP cavity. These optical losses include the Fresnel reflection from the fiber-air interfaces, the divergence of the exit beam from the lead-in fiber, and the optical absorption inside the cavity. In a low finesse FP cavity, the dominant loss is caused by the divergence angle. The loss is also a function of the cavity length. As such, one expects that the fringe visibility of the sensor is also a function of the cavity length.

Murphy *et al*. [23] described a simple plane-wave method to theoretically model the fringe visibility of an EFPI sensor as illustrated in Fig. 2.2. In this model, the output light from the SMF was considered as a diverging plane-wave with a uniform cross-sectional intensity distribution. The two interference beams from the reflections of the air/glass interfaces of lead-in and reflecting fibers were approximated by two planes waves with electric fields of E_1 and E_2, respectively. The electrical fields of the two interference beams are given by

$$E_i = A_i \exp(j\phi_i) \quad (\text{i=1, 2}) \tag{9}$$

Given that the amplitude of E_1 reflected from the lead-in fiber endface is A_1, the amplitude of E_2 reflected from the second fiber endface can be expressed as

$$A_2 = A_1 \left\{ \frac{ta}{2aL \tan[\sin^{-1}(NA)} \right\} \tag{10}$$

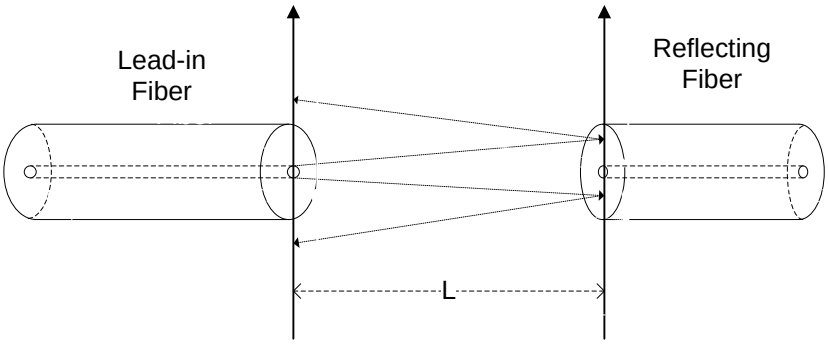

Figure 2.2. Plane wave diagram of EFPI sensor

where a is the SMF core radius, t is the transmission coefficient of the air/glass interface (~ 96%), L is the cavity length, NA is the numerical aperture of fiber, given by

$$NA = (n_{co}^2 - n_{cl}^2)^{1/2} \tag{11}$$

where n_{co} and n_{cl} are the refractive indices of the core and cladding of the lead-in fiber. The interference signal is then

$$P = A_1^2 + A_2^2 + 2A_1A_2 \cos(\phi_1 - \phi_2) \tag{12}$$

Rewriting this equation we can get,

$$P = A_1^2\left(1+\frac{2ta}{a+2L\tan[\sin^{-1}(NA)]}\cos(\frac{4\pi L}{\lambda})+\left\{\frac{ta}{2L\tan[\sin^{-1}(NA)]}\right\}^2\right) \quad (13)$$

The ratio k is given by,

$$k=\left(\frac{ta}{a+2L\tan[\sin^{-1}(NA)]}\right)^2 \quad (14)$$

Then we can write the visibility function from equation 8.

2.4. GAUSSIAN MODEL

Another method uses Gaussian beam approximation in which the output beam from a cleaved SMF is considered having a cross-sectional intensity distribution of a Gaussian profile [24]. The radial intensity profile of the light at a distance of z from the SMF endface can be approximated as [25],

$$I(r,z)=\frac{2P_0}{\pi w(z)^2}\exp\left(\frac{-2r^2}{w(z)^2}\right)=I_0(z)\exp\left(\frac{-2r^2}{w(z)^2}\right) \quad (15)$$

where r is the radial distance from the fiber center, P_0 is the total power of the light, I_0 is the maximum light intensity, and w(z) is the beam radius at the axial position z, at which the light intensity reduces to $1/e^2$ of the maximum intensity.

The beam radius of the Gaussian beam varies along the propagation direction according to the following equation

$$w(z)=w_0\sqrt{1+\left(z/z_R\right)^2} \quad (16)$$

in which, z_R is the Rayleigh length, defined by

$$z_R = \frac{\pi w_0^2}{\lambda} \tag{17}$$

where w_0 is the beam radius at the beam waist where the beam radius is at its minimum. In the case of a SMF, the Gaussian beam waist location is considered at the fiber endface (z = 0) and w_0 is taken as half of the MFD of the fiber. Once the MFD of the SMF is known, the light intensity profile at any location z from the lead-in SMF endface can be calculated.

The incident light is first partially reflected at the lead-in fiber endface. The reflected light power (P_1) can be calculated by integrating the light intensity within the core area of the lead-in fiber, given by

$$P_1 = 2\pi R \int_0^a \frac{2P_0}{\pi w_0^{\,2}} \exp\left(\frac{-2r^2}{w_0^{\,2}}\right) r dr \tag{18}$$

The remaining light enters the FP cavity and propagates a distance that equals to the cavity length L. It is then partially reflected at the reflecting fiber endface back to the FP cavity and travels the same distance L to reach the lead-in SMF endface where it is partially recouped into the fiber. The total power that is coupled into the lead-in fiber is an integration of the Gaussian beam intensity over the reception area of the fiber, which equals to the core of the lead-in SMF. As such, the light power recoupled into the lead-in fiber (P_2) is

$$P_2 = 2\pi R(1-R)^2 \int_0^a \frac{2P_0}{\pi w_{2L}^{\,2}} \exp\left(\frac{-2r^2}{w_{2L}^{\,2}}\right) r dr \tag{19}$$

where w_{2L} is the mode field radius at the distance of z = 2L, given by

$$w_{zL} = w_0 \sqrt{1 + \left(2L / z_R\right)^2} \tag{20}$$

The ratio k between P_2 and P_1 can thus be written as,

$$k = \frac{P_2}{P_1} = (1-R)^2 \frac{\int_0^a \frac{1}{w_{2L}^{\ 2}} \exp\left(\frac{-2r^2}{w_{2L}^{\ 2}}\right) rdr}{\int_0^a \frac{1}{w_0^{\ 2}} \exp\left(\frac{-2r^2}{w_0^{\ 2}}\right) rdr} \tag{21}$$

Once k is known, the fringe visibility of the EFPI sensor can be calculated as a function of the cavity length using Equation 8.

2.5. SIMULATION AND DISCUSSION

In SMF-EFPI sensor, interference between the two reflections at the lead-in fiber and reflecting fiber give rise to interference fringes at the output. The change in cavity length will cause interferometric fringe variations. Although the reflection from glass/air interface of the lead-in fiber is independent of cavity length, the intensity contributed by the reflection from the fiber mirror is strongly dependent on the cavity length, which causes the fringe visibility to decrease with an increase in the cavity length. In order to evaluate the fringe visibility degradation and estimate the maximum cavity length when the sensor remains functional, both plane-wave model and Gaussian model are used in the previous section. The simulation result of these models is shown in Fig. 2.3.

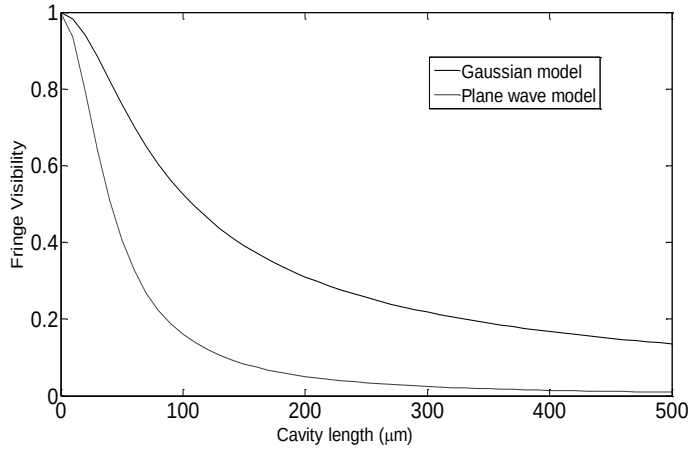

Figure 2.3. Fringe visibility of SMF-EFPI as a function of cavity length based on plane wave model and Gaussian model

Fig. 2.3 illustrates fringe visibility degradation due to cavity length increase. The interference fringes become too weak to be determined accurately when fringe visibility is small. On the other hand, SNR will also reduce as a result of decreased fringe visibility. These two factors set a limit on the dynamic range of the sensor. In SHM applications, the typical cavity length limit is 200 μm [26], beyond which the sensor doesn't function well.

From Sec 2.3, the fringe visibility is a function of fiber NA. If the NA of lead-in fiber is reduced, fringe visibility will be less sensitive to cavity length increase. Based on this assumption, fringe visibility based on plane wave model with various values of NA is plotted in Fig. 2.4. The NA is changed from 0.11 to 0.02, at a step of 0.03. As expected, the fringe visibility improves when NA is reduced.

From Fig. 2.4, by minimizing NA of lead-in fiber, it is possible to achieve higher fringe visibility. In the next chapter, we will discuss the approach to minimize the divergence angle.

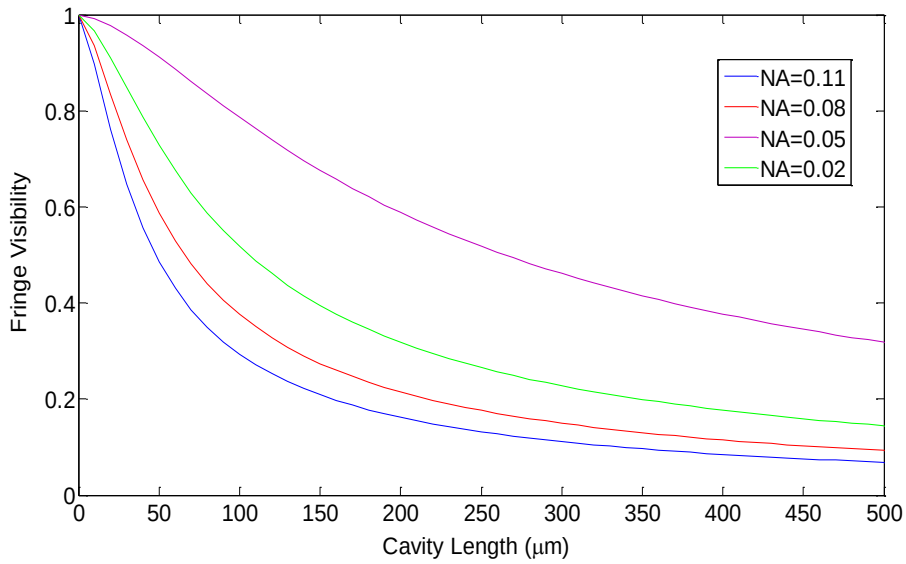

Figure 2.4. Fringe visibilities of SMF EFPI as a function of cavity length with different NA value

3. GIF EFPI SENSORS

3.1. MMF EFPI SENSOR FOR STRAIN SENSING

EFPI sensors can be constructed using either single- or multi-mode fibers [27]. Compared with SMF EFPI sensor, MMF EFPI sensors have the unique advantage of high light coupling efficiency. This is because a MMF has a large core which provides a large reception area for the reflected light.

Researchers have studied MMF EFPI sensors and their applications in strain measurement. Perennes *et al*. analyzed MMF EFPI sensors with geometrical-optics theory, in which the output light from MMF is modeled as light rays with different divergence angles [28]. Han *et al*. theoretically analyzed MMF EFPI sensors based on electromagnetic wave propagation, and modeled the electrical field by a set of guided modes with a certain power distribution and random phase relationship [29]. The feasibility of using an embedded MMF EFPI strain sensor was demonstrated by Liu *et al*., where the EFPI sensor was shown to operate in a predicable manner under quasi-static, dynamic, tensile and compressive loading [26].

However, MMFs have large NA. As a result, the fringe visibility of a traditional MMF-EFPI decreases even more rapidly as a function of the cavity length based on equation 14. Therefore, it is expected that a conventional MMF-EFPI sensor would have a dynamic range even smaller than that of a SMF-EFPI.

There are two types of MMFs: the step-index MMF (SI-MMF) and Graded-index MMF (GI-MMF). As shown in Fig. 3.1, The SI-MMF has an abrupt refractive index change at the core-cladding interface, resulting in a large NA. The GI-MMF, however, has a core refractive index decreasing gradually along its radial direction from the center point, as illustrated in Fig. 3.2. The core refractive index n(r) of GIF is a function of the radial position r, and the cladding refractive index is a constant n. The highest value of n(r) is $n(0)=n_2$, and the lowest value occurs at the core radius r=b, $n(b)=n_3$, The refractive-index profile is the power-law function

$$n(r) = n_2[1-\Delta(\frac{r}{b})^2] \tag{22}$$

where

$$\Delta = \frac{n_2^2 - n_3^2}{2n_2^2} \approx \frac{n_2 - n_3}{n_2} \tag{23}$$

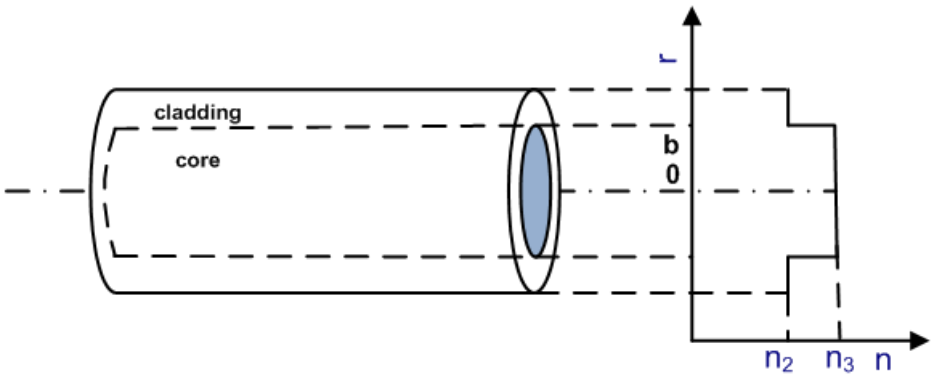

Figure 3.1. Geometry and refractive-index profile of a step-index fiber

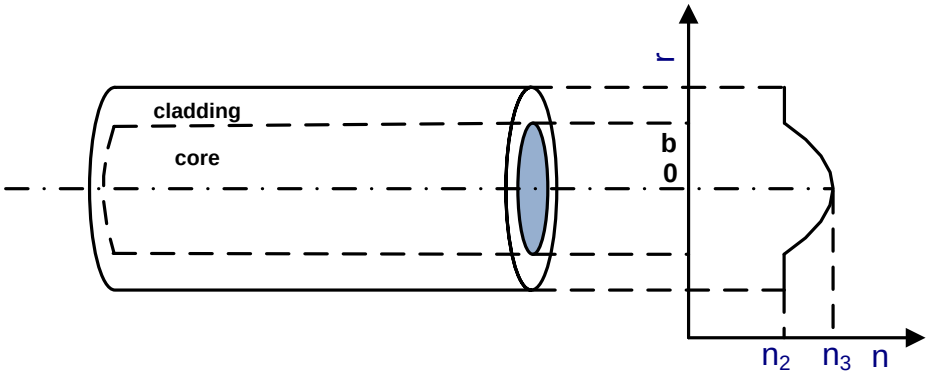

Figure 3.2. Geometry and refractive-index profile of a graded-index fiber

Light travels along the axis of GIF follows an approximately sinusoidal path [28]. The period of this sinusoidal path is defined as the pitch of the fiber. According to the

light propagation path, a GIF may be used as a collimator when its length is ¼ of the pitch, so called quarter-pitch collimator.

In this chapter, we propose a new GIF-EFPI which is constructed by splicing a quarter-pitch GIF collimator to a SMF. The use of the quarter-pitch GIF collimator can reduces the beam divergence of the exit beam and thus improve the fringe visibility at a large cavity length for extended dynamic range and improved SNR of the sensor.

3.2. PROPOSED GIF EFPI

Fig. 3.3 shows the schematic structure of proposed GIF EFPI. Its structure and packaging method are similar to that of SMF EFPI, except that a quarter-pitch GIF section is spliced to SMF at the lead-in fiber head. The reflecting fiber could be either SMF or MMF. The GIF section acts as a collimating lens, whose purpose is to reduce the divergence angle of exit light beam, and thus increase the sensor's dynamic range. It is expected that with this structure, the interference fringe visibility would increase by a large extent. In the next sections, theoretical derivation and computer simulation of its fringe visibility will be presented.

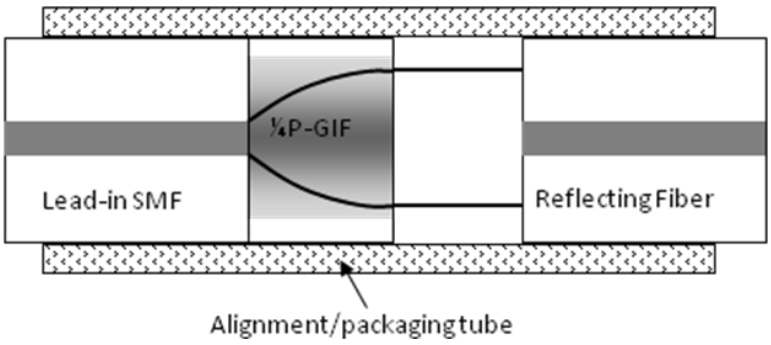

Figure 3.3. Schematic structure of proposed GIF EFPI

3.3. RAY MATRIX MODEL OF THE GIF COLLIMATOR

The theoretical model of a GIF collimator can be established based on the complex beam parameter method, which is also known as the ABCD Ray Matrix method, developed by Kogelnik *et al.* [30]. In this model, the light propagation is analyzed as a Gaussian beam. The complex beam parameter q (z) is given by

$$\frac{1}{q(z)} = \frac{1}{R(z)} - i\frac{\lambda}{n\pi w^2(z)} \tag{24}$$

where w(z) is the beam radius at position z, n is the refractive index of the medium that the light is propagating through, R(z) is the radius of curvature of the wavefronts and it evolves along z direction according to

$$R(z) = z\left[1 + \left(z_R / z\right)^2\right] \tag{25}$$

where z_R is the Rayleigh length as defined in equation 17.

At the beam waist location, the radius of curvature becomes infinity and the radius of the beam is at its minimum.

The transfer function of q between consecutive planes is given by [31]

$$q_{i+1} = \frac{Aq_i + B}{Cq_i + D} \tag{26}$$

where q_i and q_{i+1} are the complex beam parameters in plane i and plane i+1, and the terms A, B, C and D are the elements of the ray matrix. The system ray matrix is obtained by multiplying the ray matrices of the various optical components that the light propagates through, given by:

$$\begin{pmatrix} A & B \\ C & D \end{pmatrix} = \prod_{i=0}^{n} M_{i,i+1} \tag{27}$$

where $M_{i,\,i+1}$ is the ray matrix representing the optical component between the ith and (i+1) th planes.

Fig. 3.4 shows the ray matrix model schematic of a SMF spliced to a GIF collimator. Planes 1 and 2 are the two sides of the SMF/GIF interface, Planes 3 and 4 are the two sides of the glass/air interface, and Plane 5 is at the Gaussian beam waist of the output beam where the beam width is at a minimum value.

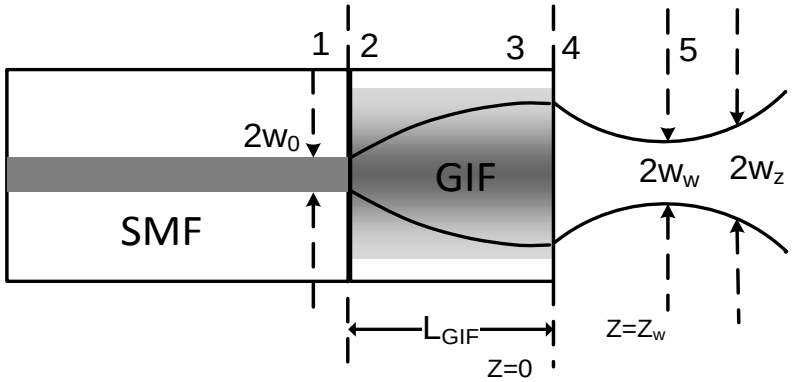

Figure 3.4. Schematic of ray matrix model of the GIF collimator

To find the Gaussian beam width of the light exiting from the GIF, we start from the SMF/GIF interface at Plane 1, where the Gaussian beam width is half of the mode field diameter of the SMF. The light propagates through Planes 2 through 4 to reach the Gaussian beam waist location (Plane 5) at a distance $z = z_w$. The ray matrices of the components that the beam propagates through include [32]:

$$M_{12} = \begin{pmatrix} 1 & 0 \\ 0 & n_1 / n_2 \end{pmatrix} \tag{28}$$

$$M_{23} = \begin{pmatrix} \cos(gL_{GIF}) & \frac{1}{g}\sin(gL_{GIF}) \\ -g\sin(gL_{GIF}) & \cos(gL_{GIF}) \end{pmatrix} \tag{29}$$

$$M_{34} = \begin{pmatrix} 1 & 0 \\ 0 & n_2 / n_0 \end{pmatrix} \tag{30}$$

$$M_{45} = \begin{pmatrix} 1 & z_w \\ 0 & 1 \end{pmatrix} \tag{31}$$

where n_1 is the core refractive index of lead-in SMF, n_2 is the core refractive index in the center of the GIF, n_0 is the refractive index of air, z_w is the distance between the GIF/air interface and the Gaussian beam waist location, and g is the focusing parameter defined as

$$g = \frac{\sqrt{2\Delta}}{b} \tag{32}$$

where Δ is the fractional index change at the core-cladding interface and b is the core radius of the GIF.

3.4. FRINGE VISIBILITY OF GIF EFPI

Based on equations 24 through 32, we can find the relative location of beam waist with respect to the lead-in fiber endface (z_w) by setting the radius of curvature $R(z_w)$ equal to infinity in equation 25, which is given by

$$w_w = \frac{w_0}{z_R n_2 g\left[\sin^2\left(gL_{GIF}\right) + \left(1/z_R n_2 g\right)^2 \cos^2\left(gL_{GIF}\right)\right]^{1/2}} \tag{33}$$

We can also find the relative location of beam waist with respect to the lead-in fiber endface, which is given by

$$z_w = \frac{n_0\left[1-\left(1/z_R n_2 g\right)^2\right]\sin\left(gL_{GIF}\right)\cos\left(gL_{GIF}\right)}{n_2 g\left[\sin^2\left(gL_{GIF}\right)+\left(1/z_R n_2 g\right)^2\cos^2\left(gL_{GIF}\right)\right]} \tag{34}$$

The radius of the Gaussian beam at an arbitrary position z is then,

$$w_z = w_w\sqrt{1+\left[\frac{\lambda(z-z_w)}{n_0\pi w_w^2}\right]^2} \tag{35}$$

As shown in Fig. 3.5, the divergence angle of the output beam is approximated as

$$\theta \cong \frac{\lambda}{\pi w_w} \tag{36}$$

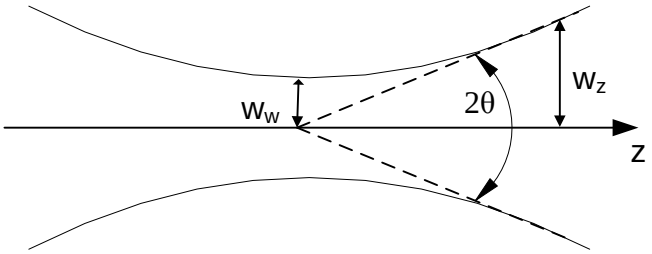

Figure 3.5. Gaussian beam divergence angle

To find the fringe visibility of the GIF collimated EFPI, we first calculate the optical power reflected at the GIF fiber endface, assuming that the SMF-GIF splice is lossless.

$$P_{1,GIF} = 2\pi R^2 \int_0^b \frac{2P_0}{\pi w_{GIF}^{\ 2}} \exp\left(\frac{-2r^2}{w_{GIF}^{\ 2}}\right) r dr \tag{37}$$

where w_{GIF} is the beam radius at the GIF endface, which can be found by setting z = 0 in equation 35, given by

$$w_{GIF} = w_w \sqrt{1 + \left[\frac{\lambda(z_w)}{n_0 \pi w_w^2}\right]^2} \tag{38}$$

To calculate the optical power of the second beam, we first calculate the radius of the Gaussian beam at the distance of z = 2L using equation 35, given by

$$w_{2L,GIF} = w_w \sqrt{1 + \left[\frac{\lambda(2L - z_w)}{n_0 \pi w_w^2}\right]^2} \tag{39}$$

The recoupled power into the GIF is calculated by integrating the reflected intensity profile at the GIF endface over the core area of the GIF, given by

$$P_{2,GIF} = 2\pi R(1-R)^2 \int_0^b \frac{2P_0}{\pi w_{2L,GIF}^{\ 2}} \exp\left(\frac{-2r^2}{w_{2L,GIF}^{\ 2}}\right) r dr \tag{40}$$

The ratio of the two interference beam intensities is,

$$k = \frac{P_{2,GIF}}{P_{1,GIF}} = (1-R)^2 \frac{\int_0^b \frac{1}{w_{2L,GIF}^{\ 2}} \exp\left(\frac{-2r^2}{w_{2L,GIF}^{\ 2}}\right) r dr}{\int_0^b \frac{1}{w_{GIF}^{\ 2}} \exp\left(\frac{-2r^2}{w_{GIF}^{\ 2}}\right) r dr} \tag{41}$$

The visibility can thus be obtained using Equation 8 after k is found.

3.5. SIMULATION AND RESULTS

From the above derivations, we can simulate the quarter-pitch GIF length and minimum divergence angle. Sec 3.5.1 will show the simulation results from ray matrix model. As verification, the FDTD simulation is also used in Sec 3.5.2.

3.5.1. Simulation Using ABCD Matrix Model. Fig. 3.6 plots the divergence angle and beam waist of the Gaussian beam as a function of the GIF length based on the ABCD ray matrix model. A commercial GIF (Corning InfiniCor 600) was employed in the simulations. From the datasheet, it has $\Delta = 1\%$ and a core radius of 25 μm. The simulation results indicate that the first minimum divergence angle occurs when the Gaussian beam waist reaches its maxima. The GIF length at this specific point is one quarter pitch length. The simulation results also predict that the minimum divergence angle is 2.2 °and the one-quarter pitch length of the GIF is 320 μm.

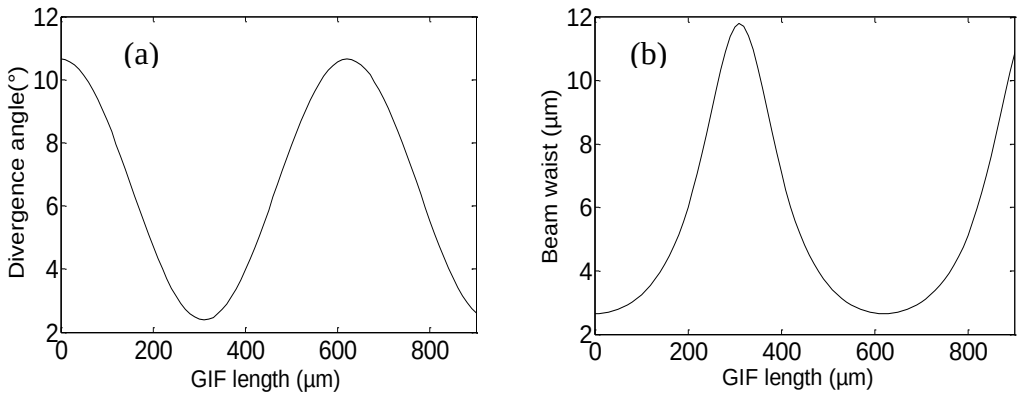

Figure 3.6. Simulation result of ray matrix model. (a) Beam divergence angle as a function of GIF length, (b) Gaussian beam width as a function of GIF length.

3.5.2. FDTD Simulation. To verify the GI-MMF based beam expander/collimator, we performed some simulations using the FDTD software (FullwaveTM by RSoft Design Group, Inc.). The simulation used commercial optical fibers made by Corning Inc. The single mode fiber was the SMF-28® with core and cladding diameter of 8.3μm and 125μm, respectively. The GI-MMF was the Infinicor-300® with core and cladding diameter of 62.5μm and 125μm, respectively. As shown in Fig. 3.7, spliced with a GI-MMF of 90μm in length, the output beam from the SMF was expanded to a collimated beam with a diameter of about 50μm. The cross-sectional intensity profile of the collimated beam also followed a Gaussian distribution as we expected.

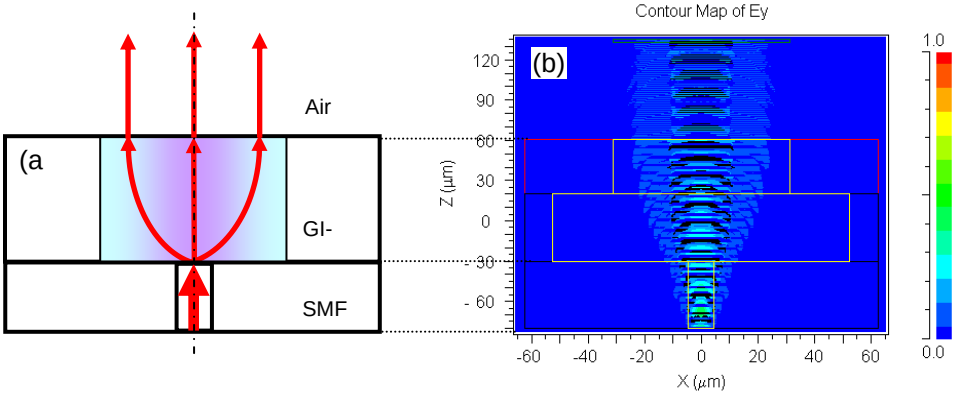

Figure 3.7. FDTD based optical simulation of the proposed GI-MMF based beam expander and collimator. (a) Device schematic, (b) FDTD simulation result

3.6. THORETICAL STUDY OF GIF EFPI VISIBILITY

Fig. 3.8 shows the simulation result of GIF EFPI and SMF EFPI visibility, including fringe visibility of the SMF EFPI using Gaussian model and plane wave model, and fringe visibility of GIF EFPI using ray matrix model. GIF EFPI could substantially

improve fringe visibility. When the cavity length is 200 μm, which is the typical upper limit of cavity length in applications for SMF, the fringe visibility of GIF EFPI is over 0.95, and that of SMF EFPI is approximately 0.35 using the Gaussian model. When cavity length reaches 500 μm, the fringe visibility of GIF EFPI is over 0.8; however, the SMF EFPI only has a visibility of 0.2 using the Gaussian model.

From this result, GIF EFPI could effectively enhance fringe visibility in theory.

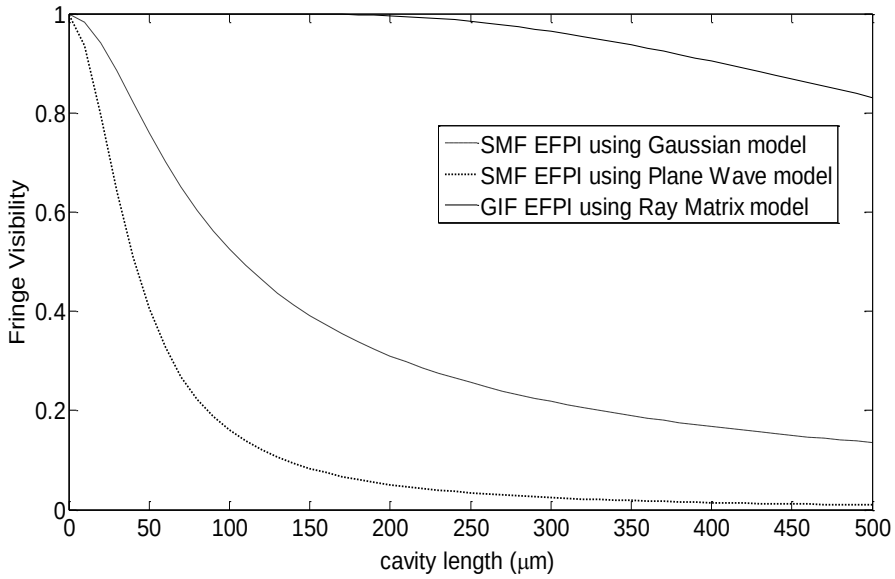

Figure 3.8. Comparison of GIF EFPI and SMF EFPI visibility by simulation

4. EXPERIMENTS AND RESULTS

4.1. GIF COLLIMATOR FABRICATION

Fig. 4.1 shows the fabrication system of GIF collimator. To fabricate GIF collimators, we first fusion spliced a section of GIF (Corning InfiniCor 600) to a SMF (Corning SMF-28e). The two ends of the spliced fiber were then fixed on two precision translation stages (Newport, PM 40276). By synchronizing the two stages using a programmed stage controller (Newport pm500-c), the spliced fiber was able to move along its axial direction with a resolution of 500 nm. A fiber cleaver (Fujikura High Precision Fiber Cleaver) was placed under the spliced fiber with its blade perpendicular to the fiber axis. By fine tuning the height of the blade, we were able to achieve a good cutting quality. A microscope was also set up to capture the image of the cleaver blade and spliced fiber as shown in Fig. 4.2(a). During the cleaving process, we first pre-strained the fiber and moved the translation stages to precisely align the GIF/SMF interface with the cleaver blade. Then we moved the GIF/SMF interface by a distance of the desired GIF length away from the blade plane. The GIF collimator fabrication was completed by triggering the cleaver blade. To evaluate the accuracy, we also measured the GIF length using a measuring microscope (Nikon MEASURESCOPE UM-2). We performed 65 cleaves. The standard deviation of the GIF length was 5.2 μm. Fig. 4.2(b) shows a microscopic image of a fiber collimator with a GIF length of 317 μm.

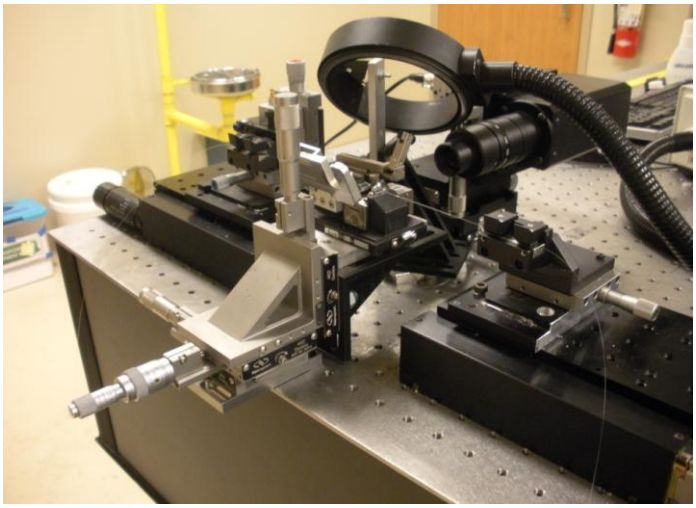

Figure 4.1. Fabrication system of GIF collimator

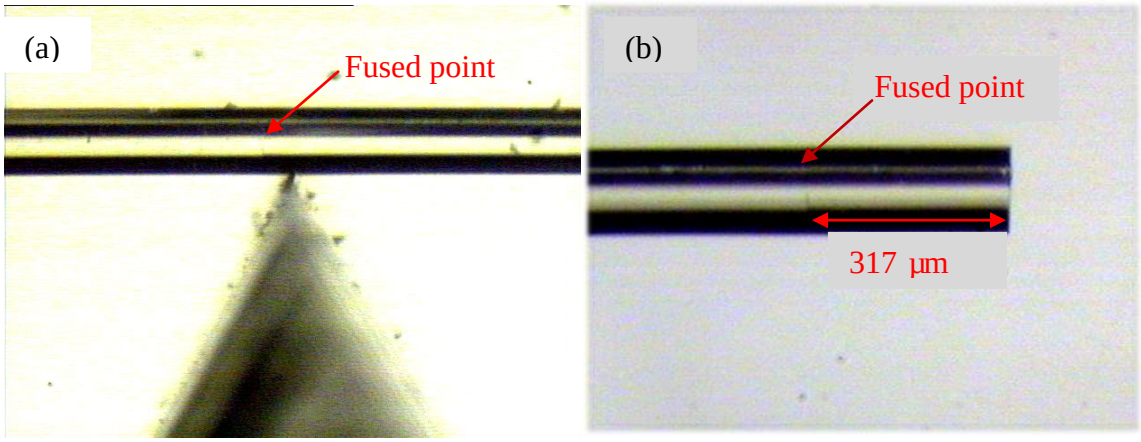

Figure 4.2. Microscopic image of fiber collimator (a) Image of the cleaver blade and fused fiber (b) Image of a cleaved GIF collimator.

4.2. DIVERGENCE ANGLE MEASUREMENT

Fig. 4.3 shows the schematic diagram of the GIF collimator divergence angle measurement setup. Fig. 4.4 is a photograph of this setup. Light from a laser source with a center wavelength of 1550 nm was launched into a SMF spliced with a GIF collimator.

The SMF-GIF collimator was fixed by a fiber holder, which was mounted on a translation stage. An infrared camera (SU320, Sensors Unlimited Inc.) was installed facing perpendicular to the GIF collimator. We adjusted the stage to ensure that the output beam profile was fully captured by the sensing area of the infrared camera. A computer was used to collect the image through a video acquisition card. In order to avoid saturation of the camera pixels, the laser power was set to -22 dBm.

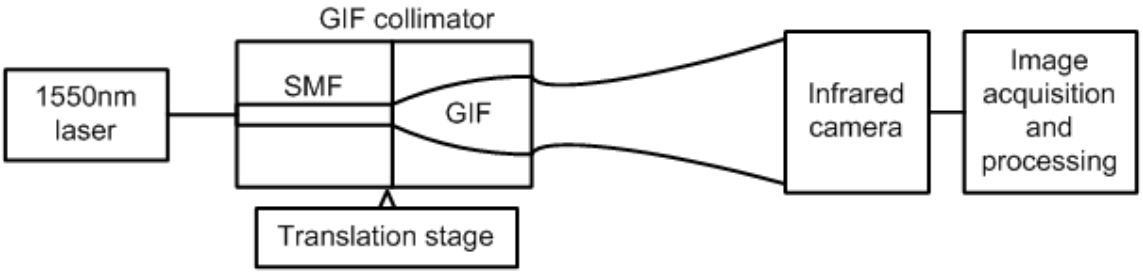

Figure 4.3 Schematic of divergence angle measurement

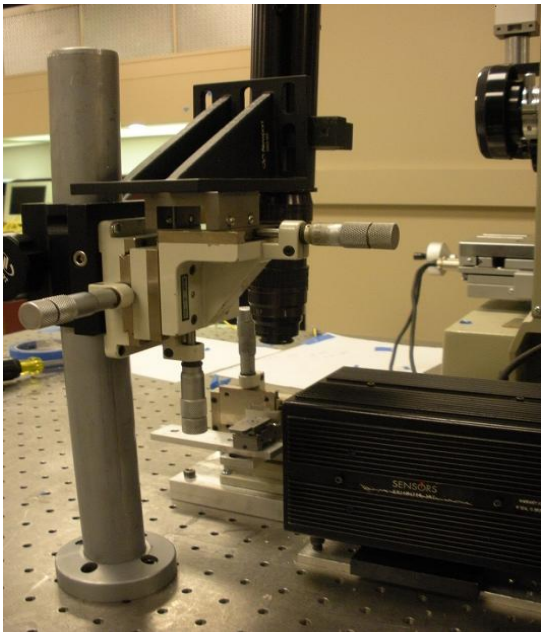

Figure 4.4. Photograph of divergence angle measurement system

The insert of Fig. 4.5 shows a representative far field IR image obtained by the infrared camera. To obtain the beam radius, we drew a horizontal line across the center pixel and plotted the grey level distribution along this horizontal line. As shown in Fig. 4.5, the grey level followed an approximate Gaussian distribution. A polynomial fit was used to smooth the distribution curve. The two points where their intensity was at the $1/e^2$ of the maximum were then calculated and the distance between these two points were taken as twice of the Gaussian beam radius.

In the far field, the Gaussian beam width grows linearly as a function of distance from the collimator. The beam radius measured by the camera increases due to beam divergence as the linear translation stage moves the collimator away from the camera. The divergence angle of the output beam can thus be calculated based on the derivative of Gaussian beam width with respect to the distance that the collimator moves according to the following equation [33]

$$\theta_{div} = \frac{w(d_2) - w(d_1)}{d_2 - d_1} \tag{42}$$

where $w(d_1)$ and $w(d_2)$ are the Gaussian beam widths at distance d_1 and d_2, respectively. To minimize the measurement error, the beam radius at multiple fiber positions can be measured. The divergence angle is then calculated based on the slope of the linear-fitted line of the beam radius as a function of the fiber positions.

To find the slope, we first recorded the images projected from the GIF collimator at 6 different positions of fiber movements. The distance between two consecutive fiber movements was 1 mm. The beam width of each position was then calculated based on the captured IR image. Fig. 4.6 shows the far field beam width as a function of the fiber movements using a GIF collimated SMF with the GIF length of 317 μm. The slope of the linear fitted line was found to be 0.0404, corresponding to a divergence angle of 2.3°. To validate the experiment setup and procedures, we also measured the beam divergence angle from a SMF using the same method. Also shown in Fig. 4.6, the measured divergence angle was 7.7 °, which agreed well with the NA of the fiber from the datasheet.

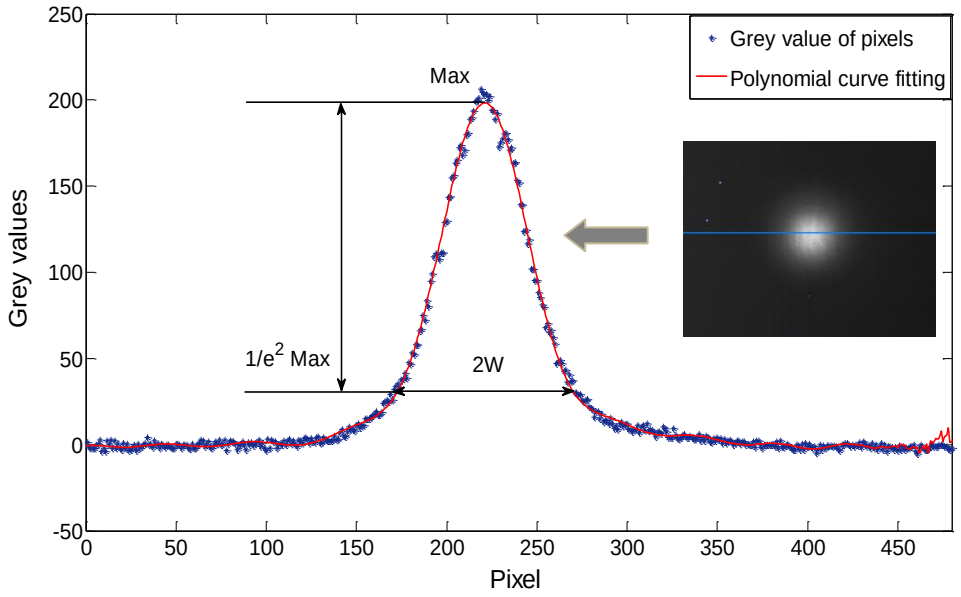

Figure 4.5. Far field intensity distribution of output beam from the GIF collimator. Insert: Far field IR image obtained by the infrared camera.

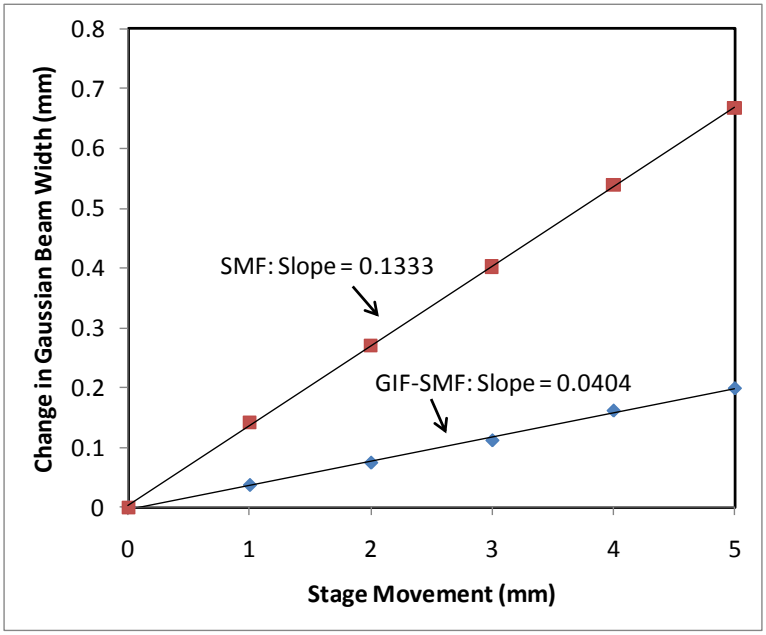

Figure. 4.6. Changes in Gaussian beam width as a function of stage movement

Fig. 4.7 plots the measured divergence angle as a function of the GIF length ranging from 20 μm to 780 μm. The ray matrix simulation result is also shown for comparison. In general, the divergence angle varied as a sinusoidal-like function of the GIF length. We curve fitted the data using a sinusoid function based on the least-square principle for a better visualization. The smallest divergence angle θ was 2.3° measured at the GIF length of 317 μm. The measurement results agreed well with the simulation predictions. In comparison, the measurement results indicated that the divergence angle could be reduced by splicing a GIF collimator with appropriate length to a SMF.

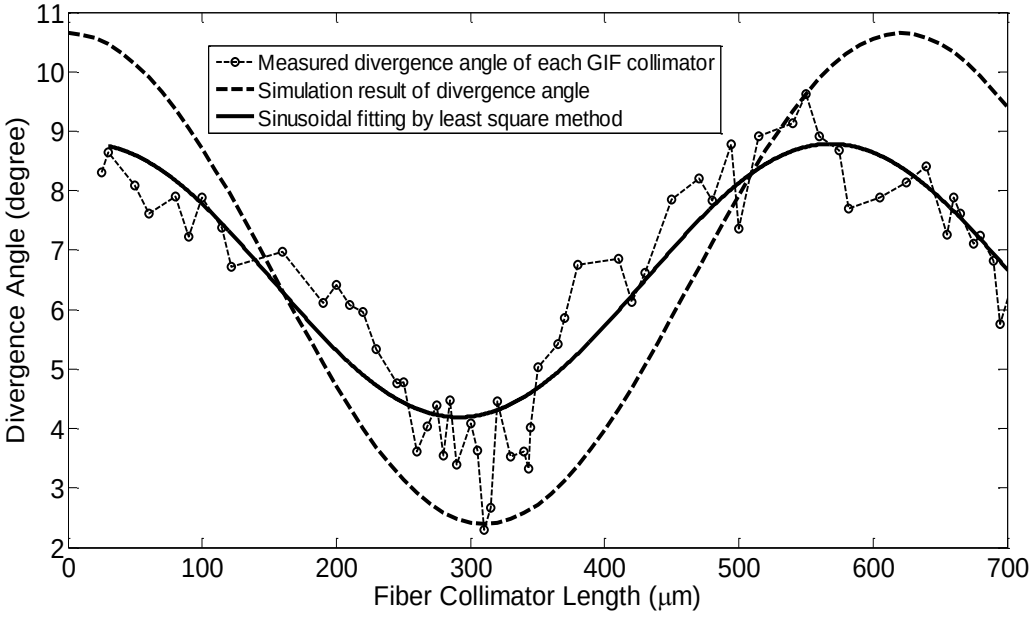

Figure 4.7. Divergence angles of the GIF collimators as a function of the GIF length

4.3. FRINGE VISIBILITY MEASUREMENT

To evaluate the fringe visibility enhancement by using a GIF collimator, both a SMF-EFPI and a GIF-EFPI with different FP cavity lengths were experimentally

investigated. A white light interrogation system is set up for fringe visibility measurement as shown in Fig. 4.8. A broadband source, with a wavelength range from 1520 to 1620nm, was made by multiplexing a C-band (AFC, BBS-1550A-TS) and an L-band (Highwave, HWT-BS-L-P) erbium-doped fiber ASE source. The broadband light excited the EFPI device through a 1×2 3dB fiber coupler. The reflected interference spectrum from the EFPI was detected by an optical spectrum analyzer (OSA, AQ6319).

The EFPI was constructed by first inserting a cleaved SMF into a hollow core glass tube with an ID of 127 μm. Epoxy was carefully used to bond the SMF and the glass tube without contaminating the cleaved fiber endface. The glass tube was mounted on a stationary block. A GIF collimated SMF (or a SMF in the case of a regular SMF-EFPI) was then inserted into the tube from the other end of the glass tube. This GIF collimator fiber was mounted on a 3-D precision translation stage through a fiber holder so that it could be moved to change the cavity length. The glass tube ensured the parallelism between fiber endfaces during the movement of the lead-in GIF fiber along its axis. Also, it provided a protection for the sensor head against environmental perturbations. A microscope was also used to assist the assembly process and estimate the cavity length. The actual cavity length was calculated based on the stage movement with a resolution of 500 nm.

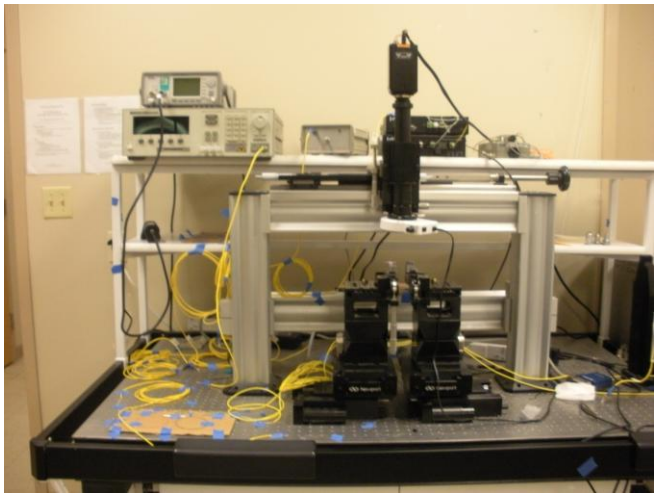

Figure 4.8. Photograph of EFPI divergence angle measurement system

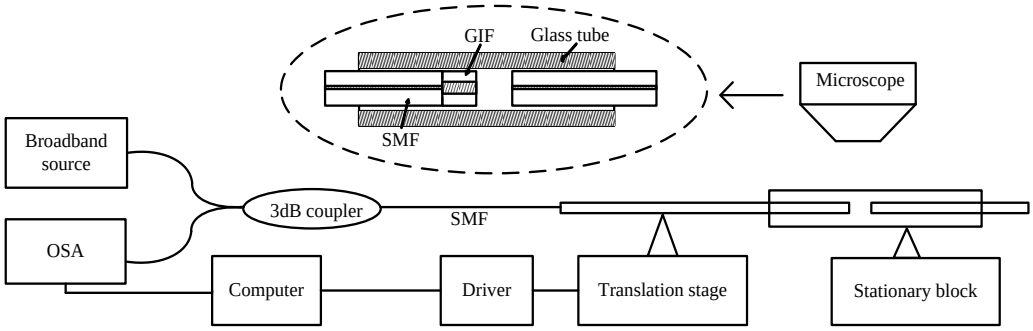

Figure 4.9. Schematic of EFPI divergence angle measurement system

In the experiments, we set the initial FP cavity length at 20 μm, and then moved the stage to increase the cavity length. The Interference spectra were recorded at different cavity length until it reached 500 μm. Fig. 4.10 shows the interference spectrum of a GIF collimated EFPI at the cavity length of 200 μm. The GIF collimator had a length of 317 μm. The interference spectrum of a SMF-EFPI at the same cavity length is also shown for comparison. The fringe contrast of the GIF collimated EFPI exceeded 13 dB (V= 0.92) while the SMF-EFPI was around 4 dB (V= 0.43), clearly indicating the improvement in fringe visibility by using a GIF collimator.

Fig. 4.11 plots the measured fringe visibility as a function of the FP cavity length of both SMF-EFPI and GIF-EFPI. The fringe visibility of both decreased as the cavity length increases, however, the former decreased much faster than the latter. At the cavity length of 500 μm, the fringe visibility dropped to about 0.2 for the SMF-EFPI, while that of the GIF-EFPI only dropped to 0.8 which was about the same of a SMF-EFPI with a cavity length of about 80 μm. Simulated fringe visibilities from previous theory are also plotted in Fig. 4.11 for reference. The theoretical fringe visibility of the SMF-EFPI using the Gaussian model fit the experimental results better than that using the plane wave model. The ray matrix model simulation result of the GIF-EFPI also fit the experiment data in the general trend. However, we did notice that the measured fringe visibilities were constantly smaller than those obtained from simulations. The deviations might be caused by non-ideal factors such as the non-perpendicular cleaving of the fiber and the axial misalignment between the lead-in and reflecting fibers. The ID of silica tube is

slightly larger than the fiber diameter, which might have caused an axial offset between the two fibers.

The experiment results demonstrated that the fringe visibility of an EFPI could be enhanced by splicing a quarter-pitch GIF onto the lead-in SMF as a collimator, which effectively reduced the divergence angle of the beam traveling inside the FP cavity. The increased fringe visibility could result in a larger SNR to improve the measurement accuracy. Besides, a GIF-EFPI could be used at a much larger cavity length since its visibility is less sensitive to the increase in cavity length than that of a SMF-EFPI. This could be a potential solution for large strain measurement in structural health monitoring, such as crack opening detection.

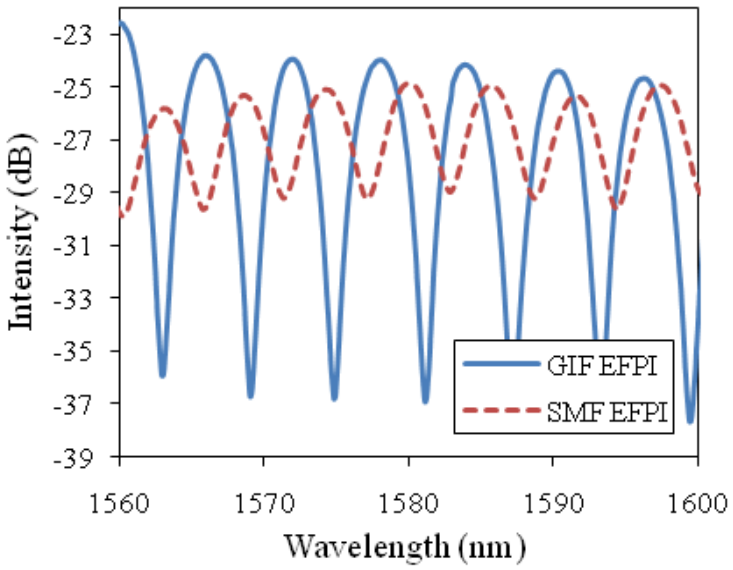

Figure 4.10. Interference spectra of the SMF-EFPI and GIF-EFPI at the cavity length of 200 μm

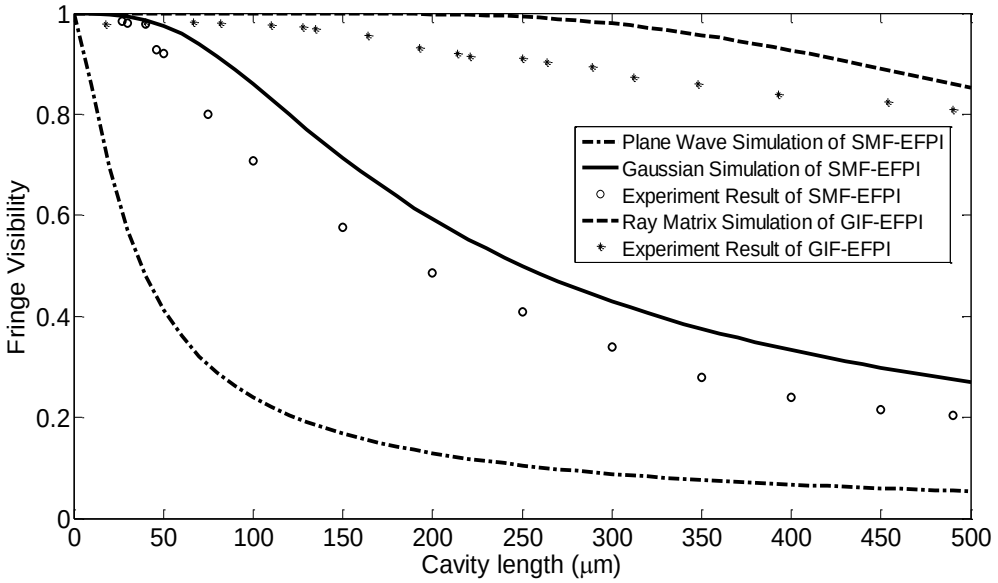

Figure 4.11. Fringe visibility comparison of the SMF-EFPI and GIF-EFP

5. CONCLUSIONS AND FUTURE WORK

5.1. CONCLUSIONS

In this thesis, we presented a visibility-enhanced EFPI by using a quarter-pitch GIF as the collimator that was fusion spliced to the lead-in SMF. The ABCD ray matrix method was used to model the GIF collimator. The simulation result predicted that a collimator could be obtained by cutting the GIF (Corning Infinicor 600) at the quarter-pitch length of 320 μm to obtain a minimum divergence angle of 2.2 º. GIF collimators were fabricated by precise fiber cleaving under a microscope with micron-level accuracy. The beam divergence angle of a GIF collimated SMF was experimentally measured as a function of the GIF length using an infrared camera and image processing at far field. The measurement results were in good agreement with the simulation results. At the GIF length of 317 μm, the measured divergence angle was 2.3°. The fringe visibility as a function of the cavity length was studied theoretically and measured experimentally for both SMF-EFPI and GIF-EFPI. The simulated fringe visibility from Gaussian beam approximation fit well with the measurement results. At the cavity length of 500 μm, the fringe visibility of the GIF-EFPI was 0.8 while that of the SMF-EFPI was only 0.2. We conclude that the fringe visibility of an EFPI can be effectively enhanced splicing a quarter-pitch GIF collimator to the lead-in SMF. The visibility enhanced GIF-EFPI provides better a SNR for applications where a large dynamic range is desired such as such as crack opening detection and large strain measurement in structural health monitoring.

5.2. FUTURE WORK

The next phase for this project is to apply the GIF EFPI sensors in structure test. We will develop an integrated fiber optic sensor network for in-situ measurements of multiple physical parameters. The sensor multiplexing and signal processing methods for simultaneous measurements of multiple physical parameters will be implemented and evaluated using EFPI sensors. We will conduct a detailed design of the proposed mesh sensor network through computer simulations. In addition to the network design, we will also investigate various means to physically protect the sensors and the fiber cables from

fire threats, including sensor packaging, sensor attachment, fiber routing, fiber hosting, and fiber deployment.

Another area of research is designing a new common-path OCT fiber probe consists of a short piece of GIF which expands and collimates the output light into a parallel beam. By using GIF as the beam expander, the fiber probe has advan very small size and easy assembly. The fiber probe could be inserted into a body cavity for imaging internal organs.

APPENDIX

Matlab code for visibility simulation:

```
clear all;
close all;
clc

wl=1.55;
n=1;
a=4.1;
w0=5.2;
NA=0.14;
t=0.96;

for s=0:10:500
   z=2*s;
k(n)=t*a./(a+z.*tan(asin(NA)));
V(n)=2*k(n)/(1+k(n)^2);

zr=pi*w0^2/wl;
wz=w0*sqrt(1+(s/zr)^2);
P=0.96^2*quad(@(r)2./pi./wz.^2.*exp(-2*r.^2./wz.^2).*r,0,a);
P0=quad(@(r)2./pi./w0.^2.*exp(-2*r.^2/w0.^2).*r,0,a);
k=P./P0;
V1(n)=2*sqrt(k)/(1+k);
n=n+1;
end

X=[0:10:500];
figure
plot(X,V);
```

```
hold on;
plot(X,V1);
hold on;

b=25;
delta=0.01;
n2=1.476;
L1=317;
n0=1;
n=1;

for s=0:10:500
   z=2*s;
g=sqrt(2*delta)/b;
ww=w0/(zr*n2*g)/sqrt((sin(g*L1))^2+(1/zr/n2/g*cos(g*L1))^2);
zw1=n0*(1-
(1/zr/n2/g)^2)*sin(g*L1)*cos(g*L1)/n2/g/(sin(g*L1)^2+(1/zr/n2/g*cos(g*L1))^2);
ws=ww*sqrt(1+(wl*(z-zw1)/pi/ww^2)^2);
P3=0.96^2*quad(@(r)1./ws.^2.*exp(-2*r.^2./ws.^2).*r,0,b);
P00=quad(@(r)1./w0.^2.*exp(-2*r.^2./w0.^2).*r,0,b);
k1=P3/P00;
V2(n)=2*sqrt(k1)/(1+k1);
n=n+1;
end

X=[0:10:500];
plot(X,V2);
hold off;
```

Matlab code for far field light intensity distribution:

```
clear all;
```

```
clc;
A_background=imread('background.bmp');
[r0 c0 d0]=size(A_background);
red0(:,:,1)=A_background(:,:,1);
red0(:,:,2)=zeros(r0,c0);
red0(:,:,3)=zeros(r0,c0);
u_red0=uint8(red0);

green0(:,:,2)=A_background(:,:,2);
green0(:,:,1)=zeros(r0,c0);
green0(:,:,3)=zeros(r0,c0);
u_green0=uint8(green0);

blue0(:,:,3)=A_background(:,:,3);
blue0(:,:,1)=zeros(r0,c0);
blue0(:,:,2)=zeros(r0,c0);
u_blue0=uint8(blue0);

red10  =red0(1:307200);
red10 =double(red10);
green10=green0(307201:614400);
green10=double(green10);
blue10 =blue0(614401:921600);
blue10=double(blue10);
light0=0.299.*red10 + 0.587.*green10 + 0.114.*blue10;

for Num_readimage =3:1:5
    url=strcat('C:\Users\Yinan\Desktop\research\zhengtai\');
    filename=strcat(url,num2str(Num_readimage),'.bmp');
    A=imread(filename);
    [r c d]=size(A);
```

```
red(:,:,1)=A(:,:,1);
red(:,:,2)=zeros(r,c);
red(:,:,3)=zeros(r,c);
u_red=uint8(red);

green(:,:,2)=A(:,:,2);
green(:,:,1)=zeros(r,c);
green(:,:,3)=zeros(r,c);
u_green=uint8(green);

blue(:,:,3)=A(:,:,3);
blue(:,:,1)=zeros(r,c);
blue(:,:,2)=zeros(r,c);
u_blue=uint8(blue);

red1  =red(1:307200);
red1 =double(red1);
green1=green(307201:614400);
green1=double(green1);
blue1 =blue(614401:921600);
blue1=double(blue1);
light=   0.299.*red1 + 0.587.*green1 + 0.114.*blue1;
light1=light(1:65535);

count(Num_readimage)=0;
result(Num_readimage)=0;
result_circle(Num_readimage)=0;
R_circle(Num_readimage)=0;
x_circle(Num_readimage)=0;
y_circle(Num_readimage)=0;
```

```
 max_light=max(light-light0);
 abs_sub=255;
 for i=1:307200
    light(i)=light(i)-light0(i);
    if light(i)==max_light
       y_circle(Num_readimage)=1+fix(i/480);
       x_circle(Num_readimage)=i-(y_circle(Num_readimage)-1)*480;
    end
 end
 count_zhengtai=0;
 x_heng=(x_circle(Num_readimage)-270):(x_circle(Num_readimage)+270);
 for j=(x_circle(Num_readimage)-270):(x_circle(Num_readimage)+270)
    count_zhengtai=count_zhengtai+1;
    light_zhengtai(count_zhengtai)=light(j+(y_circle(Num_readimage)-1)*480);
 end

 count_zhengtai_y=0;
 y_heng=(y_circle(Num_readimage)-20):(y_circle(Num_readimage)+20);
 for j1=(y_circle(Num_readimage)-20):(y_circle(Num_readimage)+20)
    count_zhengtai_y=count_zhengtai_y+1;
    light_zhengtai_y(count_zhengtai_y)=light(x_circle(Num_readimage)+(j1-1)*480);
 end
 plot(x_heng,light_zhengtai,'r');
 hold on;
xlabel('pixel');
ylabel('grey values ');
end
```

BIBLIOGRAPHY

1. E. Schedin and A. Melander, "The evaluation of large strains from industrial sheet metal stampings with a square grid," *Journal of Applied Metal Working* 4, 14-56 (1986).

2. T. Sawada and M. Sakamoto, "High resolution of large strain with Fourier phase correlation method by image sensing camera," *Steel Grips* 2, 681-685 (2004).

3. T. Youshino, K. Kurosawa, K. Itoh, and T. Ose, "Fiber-Optic Fabry-Perot Interferometer and Its Sensor Applications," *IEEE T Micro Theory* MTT-30, 1612-1621 (1982).

4. T. Wei, Y. Han, H. L. Tsai, and H. Xiao, "Miniaturized fiber inline Fabry-Perot interferometer fabricated with a femtosecond laser," *Opt Lett* 33, 536-538 (2008).

5. J. Zhang, G. D. Peng, L. Yuan, and W. Sun, "Composite-cavity-based Fabry-Perot interferometric strain sensors," *Opt Lett* 32, 1833-1835 (2007).

6. W. Wang, N. Wu, Y. Tian, X. Wang, C. Niezrecki, and J. Chen, "Optical pressure/acoustic sensor with precise Fabry-Perot cavity length control using angle polished fiber," *Opt Express* 17, 16613-16618 (2009).

7. J. R. Lawall, "Fabry-Perot metrology for displacements up to 50 mm," *J Opt Soc Am A Opt Image Sci Vis* 22, 2786-2798 (2005).

8. P. C. Beard and T. N. Mills, "Extrinsic optical-fiber ultrasound sensor using a thin polymer film as a low-finesse Fabry–Perot interferometer," *Appl Opt* 35, 663-675 (1996).

9. K. D. Oh, A. Wang, and R. O. Claus, "Fiber-optic extrinsic Fabry-Perot dc magnetic field sensor," *Opt Lett* 29, 2115-2117 (2004).

10. T. Wei, Y. Han, Y. Li, H. L. Tsai, and H. Xiao, "Temperature-insensitive miniaturized fiber inline Fabry-Perot interferometer for highly sensitive refractive index measurement," *Opt Express* 16, 5764-5769 (2008).

11. J. R. Casas, "Fiber Optic Sensors for Bridge Monitoring," *J. Bridge Eng*. 8, 362-373 (2003).

12. W. Zhao, J. Wang, A. Wang, and R. O. Claus, "Geometric analysis of optical fiber EFPI sensor performance," *Smart Mater. Struct*. 7, 907-910 (1998).

13. R. O. Clauss, M. F. Gunther, A. Wang, and K. A. Murphy, "Extrinsic Fabry-Perot sensor for strain and crack opening displacement measurements from -200 to 900 degrees C," *Smart Mater. Struct* 1, 237-242 (1992).

14. H. C. Seat and S. Pullteap, "An Extrinsic Fiber Fabry-Perot Interferometer for Dynamic Displacement Measurement," *Proc. IEEE*, International Conference on Mechatronics and Automation, 3025-3030 (2007).

15. T. K. Gangopadhyay, "Non-contact vibration measurement based on an extrinsic Fabry–Perot interferometer implemented using arrays of single-mode fibres," *Meas. Sci. Technol*. 15, 911-917 (2004).

16. D. V. Baranov, I. V. Zhurilova, S. K. Isaev, L. S. Kornienko, and A. A. Sachkov, "Fiber-optic Fabry–Perot interferometers utilizing graded-index optical waveguides," *Sov. J. Quantum Electron*. 19, 690-692 (1989).

17. M. Zickar, W. Noell, C. Marxer, and N. de Rooij, "MEMS compatible micro-GRIN lenses for fiber to chip coupling of light," *Opt Express* 14, 4237-4249 (2006).

18. Y. Mao, S. Chang, S. Sherif, and C. Flueraru, "Graded-index fiber lens proposed for ultrasmall probes used in biomedical imaging," *Appl Opt* 46, 5887-5894 (2007).

19. P. Chanclou, C. Kaczmarek, G. Mouzer, and P. Gravey, "Expanded single-mode fiber using graded index multimode fiber," *Opt. Eng.* 43, 1634–1642 (2004).

20. S. Gangopadhyay and S. Sarkar, "ABCD matrix for reflection and refraction of Gaussian light beams at surfaces of hyperboloid of revolution and efficiency computation for laser diode to single-mode fiber coupling by way of a hyperbolic lens on the fiber tip," *Appl Opt* 36, 8582-8586 (1997).

21. H. J. Bang, H. K. Kang, C. S. Hong, and C. G. Kim, "Optical fiber sensor systems for simultaneous monitoring of strain and fractures in composites," *Smart Mater. Struct.* 14, N52-N58 (2005).

22. Z. Y. Huang, "Quasi-distributed intrinsic Fabry-Perot interferometric fiber sensor for temperature and strain sensing," Ph. D. Dissertation of the Virginia Polytechnic Institute and State University (2006).

23. K. A. Murphy, M. F. Gunther, A. M. Vengsarkar, and R. O. Claus, "Quadrature phase-shifted, extrinsic Fabry-Perot optical fiber sensors," *Opt Lett* 16, 273-275 (1991).

24. V. Arya, M. de Vries, K. A. Murphy, A. Wang, and R. O. Claus, "Exact Analysis of the Extrinsic Fabry-Perot Interferometric Optical Fiber Sensor Using Kirchhoff's Diffraction Formalism," *Optical Fiber Technology* 1, 380-384 (1995).

25. H. Huang and U. Tata, "Simulation, implementation, and analysis of an optical fiber bundle distance sensor with single mode illumination," *Appl Opt* 47, 1302-1309 (2008).

26. T. Liu, D. Brooks, and A. Martin, "A multi-mode extrinsic Fabry - Perot interferometric strain sensor," *Smart Mater. Struct*. 6, 464-469 (1997).

27. M. E. Jones, J. L. Grace, J. A. Greene, T. A. Tran, V. Bhatia, K. A. Murphy, and R. O. Claus, "Multiplexed absolute strain measurement using extrinsic Fabry–perot interferometers," *Proc. SPIE* 2444, 267-275 (1995).

28. F. Pe ŕenne`s, P. C. Beard, and T. N. Mills, "Analysis of a lowfinesse Fabry–Perot sensing interferometer illuminated by a multimode optical fibe," *Appl Opt.* 38, 7026-7034 (1999).

29. M. Han and A. Wang, "Exact analysis of low-finesse multimode fiber extrinsic Fabry-Perot interferometers," *Appl Opt* 43, 4659-4666 (2004).

30. H. Kogelnik, "On the Propagation of Gaussian Beams of Light Through Lenslike Media Including those with a Loss or Gain Variation," *Appl. Opt* 4, 1562-1569 (1965).

31. R. Kishimoto and M. Koyama, "Coupling Characteristics Between Single-Mode Fiber and Square Law Medium," *IEEE Trans. Microwave Theory Tech.* MTT-30, 882-893 (1982).

32. C. Jack and W. Emekey, "Analysis and evaluation of graded-index fiber-lenses," *J. Lightwave Technol.* LT. 5, 1156-1164 (2003).

33. Y. C. Lin, "Characteristics of lensed fiber collimator with larger gradient-index lens diameter," *Microwave and Optical Technology Letters* 51, 1137-1139 (2009).

VITA

Yinan Zhang was born on February 18, 1987 in Anhui, China. In June 2008, she obtained a bachelor's degree in Department of Instrumentation Science and Opto-electronics Engineering from Beihang University, Beijing, China.

In August 2008, she enrolled at Missouri University of Science and Technology to pursue a master's degree of Electrical and Computer Engineering under the guidance of Dr. Hai Xiao. She graduated in May 2010. Her research interest is fiber optic sensors for harsh environment sensing.